Influence of humidity on performance and microscopic dynamics of an ionic liquid in supercapacitor

Naresh C. Osti,[1,*] Boris Dyatkin,[2,†] Matthew W. Thompson,[3] Felix Tiet,[3] Pengfei Zhang,[4] Sheng Dai,[4] Madhusudan Tyagi,[5,6] Peter T. Cummings,[3] Yury Gogotsi,[2] David J. Wesolowski,[4] and Eugene Mamontov[1]

[1]*Chemical and Engineering Materials Division, Oak Ridge National Laboratory, Oak Ridge, Tennessee 37831, USA*

[2]*A.J. Drexel Nanomaterials Institute and the Department of Materials Science and Engineering, Drexel University, Philadelphia, Pennsylvania 19104, USA*

[3]*Department of Chemical and Biomolecular Engineering, Vanderbilt University, Nashville, Tennessee 37235, USA*

[4]*Chemical Science Division, Oak Ridge National Laboratory, Oak Ridge, Tennessee 37831, USA*

[5]*NIST Center for Neutron Research, National Institute of Standards and Technology, Gaithersburg, Maryland 20899, USA*

[6]*Department of Materials Science, University of Maryland, College Park, Maryland 20742, USA*

(Received 25 February 2017; revised manuscript received 19 June 2017; published 11 August 2017)

We investigated the influence of water molecules on the diffusion, dynamics, and electrosorption of a room temperature ionic liquid (RTIL), [$BMIm^+$][Tf_2N^-], confined in carbide-derived carbon with a bimodal nanoporosity. Water molecules in pores improved power densities and rate handling abilities of these materials in supercapacitor electrode configurations. We measured the water-dependent microscopic dynamics of the RTIL cations using quasielastic neutron scatting (QENS). The ionic liquid demonstrated greater mobility with increasing water uptake, facilitated by the nanoporous carbon environment, up to a well-defined saturation point. We concluded that water molecules displaced RTIL ions attached to the pore surfaces and improved the diffusivity of the displaced cations. This effect consequently increased capacitance and rate handling of the electrolyte in water-containing pores. Our findings suggest the possible effect of immiscible co-solvents on energy and power densities of energy storage devices, as well as the operating viability of nonaqueous supercapacitor electrolytes in humid environments.

DOI: 10.1103/PhysRevMaterials.1.035402

I. INTRODUCTION

Electrical double layer capacitors (EDLCs) provide high charge storage densities, rapid charge/discharge rates, and large operating temperature windows [1–4]. These devices, typically, implement porous carbon electrodes [5] with high specific surfaces areas (SSAs) of over 1000 m^2/g and ordered porosities ($d_{pore,average} < 1.0$ nm) [6], which maximize capacitance of confined ions [7]. Most commercial devices use organic electrolytes, which, despite large operating voltage windows (over 2.5 V, compared to the 1.23 V operating limit of aqueous electrolytes) [8,9], are flammable and volatile [10]. In view of these shortcomings, room temperature ionic liquids (RTILs) have attracted much attention as EDLC electrolytes [11]. They are thermally and electrochemically stable [12], function as neat (solvent-free) systems [2], and may be adapted to optimal pore sizes [13,14]. Furthermore, co-solvents or solvated salts may be added to RTILs for high ion mobility [15], low viscosity [16], and high-rate handling [17]. Since energy storage devices must operate in diverse environments, including those with high humidity, it is critical to understand the impact of water on the microscopic dynamics of confined RTILs.

As ionic systems, RTILs are expected to be fairly hygroscopic [18]. For example, [$BMIm^+$][PF_6^-] absorbs 0.26 wt. % of water [19]. Interactions of RTILs with H_2O molecules [19,20] influence their transport properties and electrochemical dynamics [21]. Bulk RTILs form nanoaggregates in the absence of co-solvents [22], and water infusions accelerate aggregation [23]. Since the hydrophobicity of RTILs influences the hydrogen-bonding acidity and basicity [24], we anticipate a significant impact of water on cation dynamics in confinement due to interactions with the water molecules [20]. While electrodes and RTILs are usually thoroughly dried before electrochemical tests, actual supercapacitors cannot be devoid of water due to vapor-liquid equilibrium with water vapor in air. Therefore, it is important to understand the effect of water beyond narrowing the voltage window. Different forms of carbon are used for energy storage applications [5,25,26]. Here, as a model system, we have selected carbide-derived carbons (CDC) as supercapacitor materials. We report a correlation between electrochemical performance and the microscopic dynamics of a RTIL, (1-butyl-3-methyl-imidazolium bis(trifluromethylsulfonyl)imide, [$BMIm^+$][Tf_2N^-], confined in Mo_2C-derived CDC.

II. EXPERIMENTS AND SIMULATIONS

A. Gas sorption measurement

CDCs are synthesized via Cl_2 (g) etching of metal carbides and exhibit well-tailored nanoporosities [27]. A Quadrasorb-1 gas sorption analyzer (Quantachrome Instruments, USA) was used to measure the specific surface area (SSA) and porosimetry of empty and [$BMIm^+$][Tf_2N^-]-filled Mo_2C derived carbon (CDC) via N_2 gas adsorption and desorption. Measurements were conducted at 77 K (in a liquid nitrogen coolant bath). The Brunauer-Emmett-Teller (BET) SSA was calculated from the 0.05–0.30 P/P_0 adsorption regime [28]. Quenched-solid density functional theory (QSDFT) calculations, which were performed with a Quadrawin instrument

*Corresponding author: ostinc@ornl.gov

†Current address: U.S. Naval Research Laboratory, Washington, DC 20375, USA.

package, derived the DFT-modeled SSA, cumulative pore volume, and pore size distribution [29]. DFT calculations used solely the adsorption branch.

B. Electrochemical measurements

CDC powders (not filled with either water or the [$BMIm^+$][Tf_2N^-]) were rolled into electrode films according to a well-established procedure. CDC powders were mixed with a 60 wt. % dispersion of PTFE in water (Sigma-Aldrich) in excess ethanol to create a 95 wt. % carbon/5 wt. % binder slurry. The solution was stirred for 12–24 h under no heating. After the ethanol evaporated, the resulting slurry was ground with an agate mortar and pestle to homogenize the mixture and stretch the polymer fibers around the particles. Finally, CDC films were rolled to a 150 μm thickness using a mechanical rolling mill (Durston Mills, UK). Hole punches excised 12 mm disk electrodes from resulting sheets; typical electrodes weighed 6.1–6.5 mg and showcased 5.4 mg cm^{-2} mass loading densities. All electrodes were dried under low vacuum for 24 h prior to electrochemical testing. We exposed CDCs and RTILs to water vapors for different lengths of time to control the water content. To add water to the empty pores of CDCs, the electrode disks were subjected to H_2O evaporation using the desiccator system that is described below in Sec. II C. All electrodes were tested in two-electrode "pouch"/"sandwich" cells. Excess [$BMIm^+$][Tf_2N^-], which had been kept in a dry, Ar-filled glovebox prior to experiments, was added to either the "dry" or H_2O-containg electrodes. Electrodes were pressed against carbon-coated aluminum current collectors (Exopack), and two layers of 3501 Celgard® separator were inserted between each electrode. A VMP3 potentiostat (Bio-Logic, Inc.) was used for all electrochemical measurements.

Electrochemical impedance spectroscopy (EIS) measurements involving a dampening sinusoidal voltage oscillation with 10 mV amplitude centered on 0.0 V was used [30]. The technique probed frequencies in the 200 kHz to 10 mHz regime. The equivalent series resistance (ESR), which is defined as the Re(Z) values at which $-$Im(Z) values equated to 0.0, account for intrinsic electrical resistance of the supercapacitor cell and occurs at high EIS frequencies. The charge transfer resistance, which is the semicircular regime at mid-to-high frequencies, accounts for interfacial electron transport resistance between the electrode and the current collector. The τ time constant (i.e., the RC constant) is defined as the EIS ("knee") frequency at which the impedance phase angle $(Z) = -45^\circ$; it signifies the transition from resistance-dominated to capacitive-dominated impedance. The mid-frequency ionic impedance regime is defined as Re(Z) region between the charge transfer resistance and the knee frequency [31,32]. Cyclic voltammograms (CVs) were carried out using 0.5–1000 mV s^{-1} sweep rates in the 0.0–1.0 V electrochemical potential windows.

In order to evaluate the natural charge distribution of the working electrode (WE) and counter electrode (CE), several standalone cells operated in a three-electrode cell. The masses of the WE and CE were identical, and an Ag/AgCl silver wire (Ag chlorinated with HCl) acted as a quasireference electrode. It was set at the open circuit potential (OCP) and measured the potential difference between the WE and OCP and the CE and the OCP. However, this operation, which cycled the cell from a WE-CE net potential difference of 0.0 to 1.0 V (similar to the two-electrode operation shown in all other results), independently measures charge accumulation and the voltage window of each electrode. To allow a proper symmetrical comparison (i.e., a mirror image), the current shown for the CE was multiplied by -1 for all three cells [33]. The results from these measurements are specifically discussed in Fig. 2(b) and Table II.

C. Sample preparation for quasielastic neutron scattering (QENS) measurements

1-butyl-3-methyl-imidazolium bis(trifluromethanesulfonyl)imide ([$BMIm^+$][Tf_2N^-]) synthesized as described by Hillesheim *et al.* [34] was added into the pores of CDC using the previously described vacuum infiltration process [35,36]. Approximately 5.0 g of the RTIL were dispersed in a glass beaker in acetonitrile (99.5+% purity, Fischer Scientific). Based on the cumulative pore volume (1.86 $cm^3 g^{-1}$) of CDC, as well as the bulk density of [$BMIm^+$][Tf_2N^-] ($\sim$1.5 g cm^{-3}), a measured amount of the CDC powder was added to the solution in a ratio that would allow the RTIL to occupy 100% of its pore volume. The slurry was stirred (with a magnetic stir bar) at room temperature to allow acetonitrile to evaporate. Once visible liquid disappeared, the resulting powder dried under a low vacuum (0.01 Torr) at 100 °C for 24 h. Finally, to ensure uniformity, the powder was ground up in an agate mortar.

CDC + [$BMIm^+$][Tf_2N^-] samples were loaded into standard aluminum QENS sample holders of 0.25 mm thickness and left open in a plastic desiccator. A dish with excess D_2O (purchased from Sigma Aldrich) was placed next to the samples in the desiccator. The entire system was sealed and outgassed for 5 min to create a low vacuum. It was left to sit for 4, 8, or 10 h. Each sample holder with [$BMIm^+$][Tf_2N^-]-filled CDC sample was weighed prior to and after D_2O vapor exposure. A baseline reference sample was sealed in an inert environment in an Ar-filled glovebox and was, therefore, devoid of water.

D. Classical molecular dynamics (MD) simulations

To model ionic liquids confined in CDCs, a slit pore consisting of two parallel three-layer graphene sheets was constructed. Pore walls were separated by 2.5 nm, defined as the separation distance between planes of carbon atoms. The cross-sectional area of the pore was 2.5 nm × 5.5 nm. On either side of the pore was a bulk region of volume 4.0 nm × 4.0 nm × 5.5 nm, which allowed for density equilibration in the pore and molecules to sample interactions in both bulk and confinement. Because the QENS signal is believed to depend primarily on fluid behavior in mesopores, micropores were not considered in this model. All MD simulations were performed with the MD software package GROMACS 5.0.8 [37]. Ionic liquid molecules were described with the force field of Lopes *et al.* [38,39], which is similar to OPLS but specifically tuned for ionic liquids, including [$BMIm^+$][Tf_2N^-]. Charges were scaled by a factor of 0.8 to better describe transport properties [40]. Water molecules were described with the TIP3P model

TABLE I. Concentrations and number of molecules used in MD simulations.

Water concentration (mole fraction)	IL pairs/water molecules
0.203	472/120
0.382	461/285
0.482	452/420
0.602	436/660
0.792	383/1455

[41]. A time step of 1 fs and the "v-rescale" thermostat [42] with a time constant of 1 ps were used throughout. Carbon atoms making up the graphitic slit pores were fixed in place. All nonbonded interactions were computed with a cutoff of 1.1 nm. Electrostatic interactions were computed with the PME method, using a real-space cutoff of 1.1 nm and a Fourier grid spacing of 0.1 nm. All bonds were constrained using the LINCS algorithm. The concentrations and number of molecules used are shown in Table I.

Pristine graphene is highly hydrophobic, yet CDCs are hydrophilic [43] because of structural and chemical defects on the surfaces of pore walls. To simply model this water-CDC wall interaction, the energetic coefficient of the water-carbon interaction $\varepsilon_{\text{water-wall}}$ was doubled. Other cross interactions were not changed. Initial configurations for each system were generated with PACKMOL [44]. Because PACKMOL relies on geometric constraints and does not consider energetics, the first step in each simulation was to perform an energy minimization. Then, systems were annealed by heating to 600 K over 1 ns, holding at 600 K for 3 ns, and then cooling to 300 K over 5 ns. Then, a 30 ns production run of NVT simulation at 300 K was performed. Ion diffusivities were computed using the 3D Einstein diffusion equation. Region-specific diffusivities were computed by slicing the last 20 of the 30 ns trajectory into 200 slices of 100 ps length. Ion selections were updated at the beginning of each slice and the final MSD, from which the diffusivity was computed, was generated by averaging the MSD from all slices. Cations are separated into "wall" and "center" groups by their position in the pore. Cations with a center of mass less than 0.75 nm from the pore walls make up the wall region and cations with a center of mass farther than 0.75 from the pore walls are in the center region.

III. RESULTS AND DISCUSSION

CDCs are synthesized via Cl_2(g) etching of metal carbides and exhibit well-tailored nanoporosities [27]. This carbon exhibits slitlike pore structures with a high SSA (2275 $m^2 g^{-1}$) and a bimodal pore size distribution (0.78 and 3.10 nm diameter pores, as shown in Fig. 1(a) [45]. After loading with [$BMIm^+$][Tf_2N^-], the SAA decreased to 0.568 $m^2\,g^{-1}$ [Fig. 1(b)], suggesting almost complete filling of the CDC pores.

We observed the impact of water adsorption on the electrochemical performance of the [$BMIm^+$][Tf_2N^-] confined in the CDC. H_2O vapor was added to the electrode films (5.8 mg each; 95 wt. % CDC, 5 wt. % PTFE binder) for 0, 2, and 4 h. The 2-h exposure resulted in a 3.6 wt. % of water adsorbance

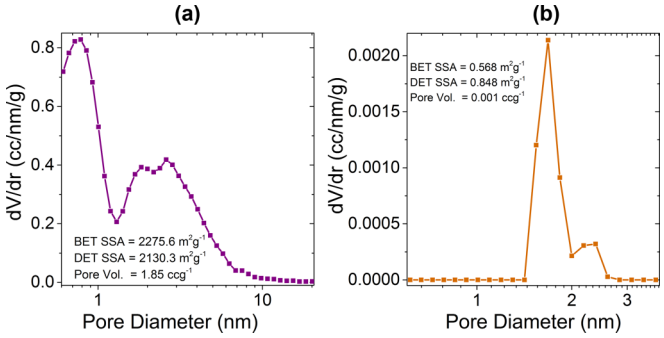

FIG. 1. Gas sorption isotherms of the oxidized bimodal CDC showing the available surface area along with the total pore volume (a) before filling the IL and (b) after filling the IL

(~0.5 mol H_2O per mol of [$BMIm^+$][Tf_2N^-] in pores) and the 4-h exposure yielded a 17.8 wt. % (~2.7 mol H_2O per mol of IL) of water uptake. Note that the time-resolved H_2O adsorption rates into CDC films did not proceed with the same kinetics as the RTIL-filled CDCs for QENS experiments (discussed later), since the former did not initially contain any [$BMIm^+$][Tf_2N^-] and included a hydrophobic polymer on their surfaces. However, this approach introduced comparable H_2O infusions into the pores and allowed us to investigate the influence of water molecules on the ion dynamics under applied potentials.

Figure 2 shows the rate handling abilities, capacitance, and electrosorption dynamics of [$BMIm^+$][Tf_2N^-] electrolyte filled CDC electrodes as a function of water content. H_2O-containing pores demonstrated greater rate handling abilities of [$BMIm^+$][TF_2N^-] in the 0.5–50 mV s^{-1} sweep rate range [Fig. 2(a)]. Since the cells were cycled within the stability window of an aqueous electrolyte (1.0 V), none of the cells demonstrated any irreversible breakdown under high potentials. Furthermore, at low sweep rates, the CVs exhibit ideal, rectangular shapes [Fig. 2(b)], and confirm the absence of any side reactions between H_2O and the RTIL. As shown in the cyclic voltammograms (CVs) in Fig. 2(d), the electrode with the highest amount of adsorbed water in the pores (4.0 h of H_2O vapor exposure) offers higher capacitance (65 F/g at 10 mV/s) than the dry electrode (60 F/g). The advantage of H_2O-filled pores becomes even more apparent at higher sweep rates; at 50 mV/s [Fig. 2(e)], CDC with the highest water content has a gravimetric capacitance (C_{sp}) of 49 F/g, as compared to its dry counterpart's 44 F/g. C_{sp} is calculated from the discharge segment of each CV and is derived via the following equation [46]:

$$C_{sp} = 2\int_{V_0}^{V_f} \frac{I}{\frac{dV}{dt} m_{WE} V_W} dV. \quad (1)$$

Equation (1) denotes the vertex potentials as V_0 and V_f, mass of a single electrode as m_{WE}, and the 1.0 V voltage window as V_W. The Randles-Sevcik coefficient (x) was calculated from CVs using the following equation relating peak current (I), charge transfer coefficient (n), Faraday constant (F), SSA (A), molar RTIL concentration (c), diffusion constant (D),

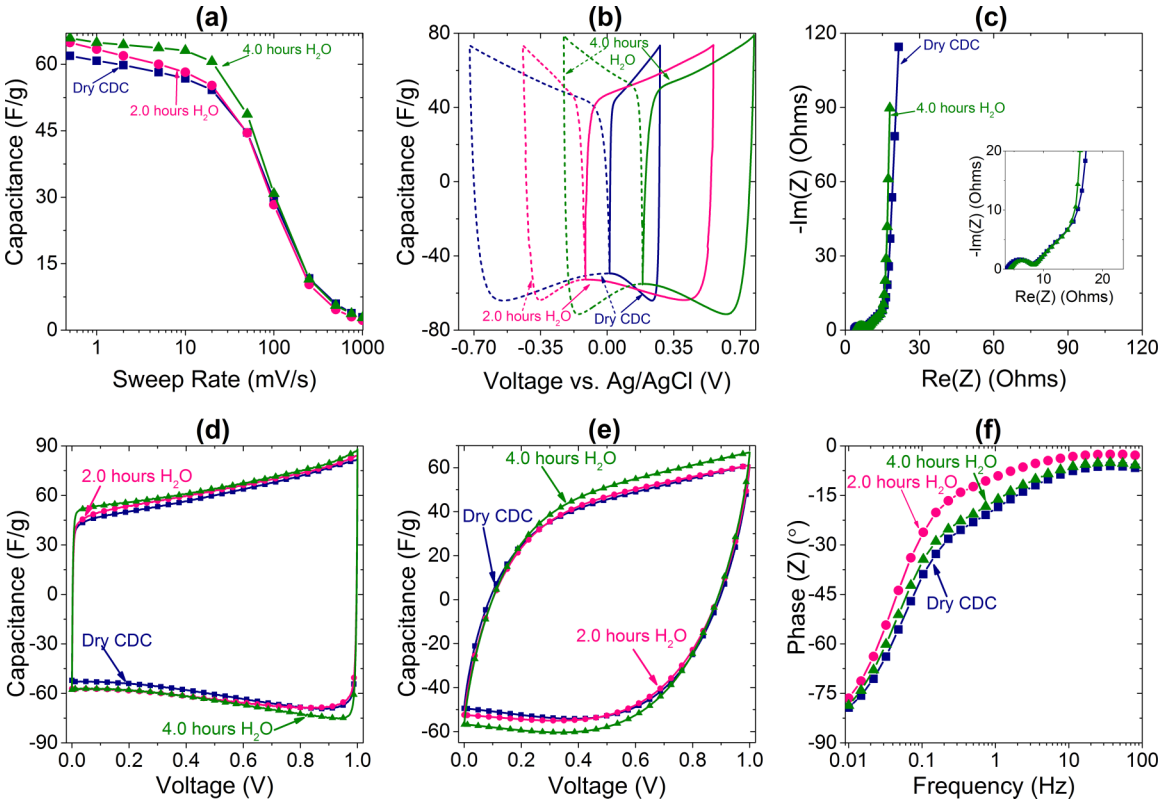

FIG. 2. Electrochemical performance of $[BMIm^+][Tf_2N^-]$ in CDC as a function of H_2O exposure time. (a) Rate handling comparison for CDCs over the entire 0.5–1000 mV/s sweep rate range. (b) Three-electrode quasireference measurements with symmetrical electrodes, carried out at 10 mV/s (summarized in Table II). (c) Nyquist plot. The inset is the zoomed in region of high-frequency impedance spectra. (d) Two-electrode cyclic voltammograms measured using a 1.0 mV/s sweep rate, as compared to those measured at (a). (e) 50 mV/s sweep rate. (f) Bode impedance plot that compares the impedance phase angle as a function of oscillating frequency.

temperature (T), gas constant (R), and the scan rate (v) [47]:

$$I = 0.4463\,(n\,F)^{1.5} A\,c \left(\frac{D}{RT}\right)^{0.5} v^{x}. \qquad (2)$$

Equation (2) was used to fit data from different sweep rates to derive values of x for each system. x values that approached 1.0 values suggest ideal capacitor behavior, whereas values of x near 0.5 indicate diffusion-limited systems. The calculated Randles-Sevcik coefficient [47] shows similar yet slightly lower diffusion limitations of the RTIL in H_2O-filled pores ($RS_{coeff} = 0.94 \pm 0.01$ at 4.0 h H_2O exposure compared to dry CDC pores with $RS_{coeff} = 0.93 \pm 0.01$).

As shown in Fig. 2(b), equilibrium charge accumulation of WE and CE are different for each system and depend on the amount of water infiltrated into the pores. The summary of different voltage windows and resulting charge accumulation are shown in Table II.

The cell devoid of any H_2O primarily favored electropotential-driven accumulation of $[BMIm^+]$ in the CE. Subsequently, relatively low anion electrosorption into the positive electrode limited its overall capacitance ($C_{total} = 10.4\,F\,g^{-1}$). However, samples with H_2O molecules in the pores demonstrated a relatively greater affinity to electrosorb the $[Tf_2N^-]$ anion. The WE electrode accumulated a greater amount of charge for the 2.0 and 4.0 h H_2O exposures, which, subsequently, yielded respective C_{total} values of 11.4 and $14.1\,F\,g^{-1}$. More importantly, however, was the fact that infiltrated water molecules balanced the relative charge distribution and equalized of the voltage window of the WE and CE. While the dry CDC WE stored 2.7 times as much charge as the CE, the 2.0 h H_2O CE/WE charge distribution

TABLE II. Charge accumulation (as calculated from the discharge sweeps), the net potential window (calculated as the difference between the vertex potential and the OCP of each electrode), and resulting capacitance of each WE and CE tested for the electrochemical systems in a three-electrode configuration. Electrochemical measurements shown in Fig. 2(b) were used to derive these values. Sweep rate was $10\,mV\,s^{-1}$.

Electrode	WE charge ($C\,g^{-1}$)	WE voltage window (V)	WE capacitance ($F\,g^{-1}$)	CE charge ($C\,g^{-1}$)	CE voltage window (V)	CE capacitance ($F\,g^{-1}$)	Total Capacitance ($F\,g^{-1}$)
Dry CDC	3.8	0.27	14.3	28.2	0.73	38.4	10.4
2.0 h H_2O	24.5	0.67	36.9	5.4	0.23	16.4	11.4
4.0 h H_2O	19.7	0.59	33.5	10.3	0.41	24.7	14.1

ratio was 2.2, while the 4.0 h CE/WE ratio dropped to 1.3. Improved electrolyte dynamics, which facilitate both ion and counterion electrosorption rates, likely influenced this increase in symmetrical operation of WE and CE. As shown in Fig. 2(b), as H_2O content in pores increases, the charge distribution in cells becomes more symmetric [12]. While dry CDC cells favor larger charge accumulation on the counterelectrode (i.e., [$BMIm^+$]), H_2O molecules in confinement likely drive away some of the hydrophobic cations and distribute charge accumulation more evenly between the two electrodes. Recent results have suggested that electrode symmetry and subsequent charge distribution significantly influence the operating voltage window [12], and water molecule infiltration may also be considered as an electrode design tool in an effort to adjust electrolyte stability.

Figure 2(c) compares the electrochemical impedance of [$BMIm^+$][Tf_2N^-] dynamics and resistance in cells with different H_2O water contents. H_2O negligibly affected the intrinsic electrical resistance of the electrodes; this is shown by similar Re(Z) values [at –Im(Z) = 0.0 Ω] for CDCs after 0.0 or 4.0 h of H_2O vapor exposure. However, the almost identical (∼4.5 Ω) charge transfer resistance (semicircular high-frequency region) [32] suggests that the electrode/current collector interface is not affected by H_2O content in the pores. Furthermore, ionic impedance [31] decreases with greater H_2O content in pores: while it is 8.8 Ω for dry CDC, it is 7.5 Ω for 4.0 h H_2O-exposed CDC. Finally, the impedance phase angle Fig. 2(f) shows nearly identical phase offsets for all CDCs at low frequencies. However, the impedance of the cell with the highest water content becomes dominated by the capacitive contribution at higher frequencies, therefore suggesting the improved dynamics of [$BMIm^+$][Tf_2N^-] in H_2O-containing pores.

Microscopic dynamics of the [$BMIm^+$][Tf_2N^-] confined in CDC were investigated using QENS. With a backscattering spectrometer [48], we measured the elastic intensity as a function of temperature. Similar to an ionic liquid confined on micropores [49], the spectrum presented in Fig. 3(a) does not show any abrupt changes, indicating the absence of phase transitions and confirming complete confinement of the ionic liquid inside the pores.

QENS experiments were performed on a NG-2 high flux backscattering spectrometer (HFBS) [50] at the National Institute of Standard and Technology (NIST) using neutron wavelength $\lambda_0 = 6.27$ Å and energy $E_0 = 2.08$ meV. Data were collected using Si (111) analyzer crystals, from 16 detectors that access the Q ranges of 0.25 to 1.74 $Å^{-1}$. Instrument dynamic energy range of ±15.5 μeV was used during the measurement. Data were collected from each sample for about 8 h to have adequate statistics. Sample temperature was controlled using a standard top loading closed cycle refrigerator. QENS spectra were collected from the sample exposed to D_2O vapors for 0.0, 4.0, 8.0, and 10.0 h at 290 K. D_2O was used to take advantage of different hydrogen and deuterium incoherent neutron scattering cross sections [51], in order to probe exclusively hydrogen-bearing RTIL cations. Sample-specific resolution was measured from each sample at 4 K. The background originated from the CDC was also measured for the same amount of time and was

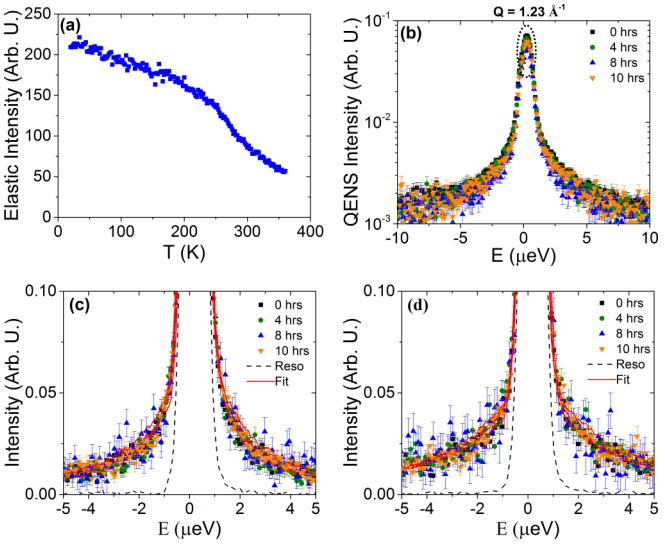

FIG. 3. (a) Elastic neutron scattering intensity of the [$BMIm^+$][Tf_2N^-] confined in bimodal CDC as a function of temperature. (b) Mass normalized $S(Q, E)$ of all samples showing a drop (as marked by a dotted ellipsoid) in intensity after water exposure. QENS spectra at (c) $Q = 0.68$ $Å^{-1}$ and (d) $Q = 1.16$ $Å^{-1}$ at 290 K. The symbols correspond to the data collected at different exposure times as indicated in the figure. Solid lines are fit using a Lorentzian function and the dotted lines (black) show the instrument resolution measured at 4 K. Data has been normalized to the highest intensity for the purpose of comparison and truncated at 0.1 arbitrary units for clarity. Error bars throughout the text represent one standard deviation.

subtracted. Data were reduced and normalized to vanadium standard using DAVE [52] software. Mass normalized QENS intensity presented in Fig. 3(b) shows a decrease in intensity after D_2O exposure suggesting a broadening of quasielastic spectra with an increase in D_2O exposure time. Those 16 detectors data were grouped to eight bins for further analysis. Two representative QENS spectra at $Q = 0.68$ $Å^{-1}$ and $Q = 1.16$ $Å^{-1}$ are shown in Figs. 3(c) and 3(d), respectively. The results show quasielastic (QE) broadening of the spectra with respect to the instrument resolution.

Since only the cation in [$BMIm^+$][Tf_2N^-] has hydrogen, the QENS signals originate predominantly form cation dynamics. The dynamic scattering function $S(Q,\omega)$, which is measured during QENS experiment, is given by [53]

$$S(Q,\omega) = \{A_0(Q)\delta(\omega) + [1 - A_0(Q)]S_{QE}(Q,\omega)\} \otimes R(Q,\omega), \quad (3)$$

where ω is the angular frequency related to energy transfer as $E = \hbar\omega$. $A_o(Q)$ is the elastic incoherent scattering originating from immobile hydrogen [54]. $\delta(\omega)$, $S_{QE}(Q,\omega)$, and $R(Q,\omega)$ are Dirac delta, quasielastic, and instrument resolution functions, respectively. A flat background was added during data analysis to incorporate the motions that are outside the instrument dynamic energy window. The $S_{QE}(Q,\omega)$ in Eq. (3) was modeled to a single Lorentzian function to probe the

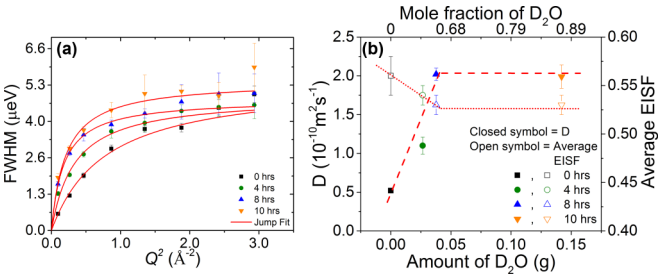

FIG. 4. (a) FWHMs extracted from a single Lorentzian fit of $S(Q, E)$ of the confined [$BMIm^+$][Tf_2N^-] as a function of D_2O exposure time are fitted using a jump diffusion model [represented by solid lines (red)]. (b) Corresponding diffusion coefficients of cations (left y axis) and average elastic incoherent scattering fraction (right y axis). The dotted lines are a guide to the eye.

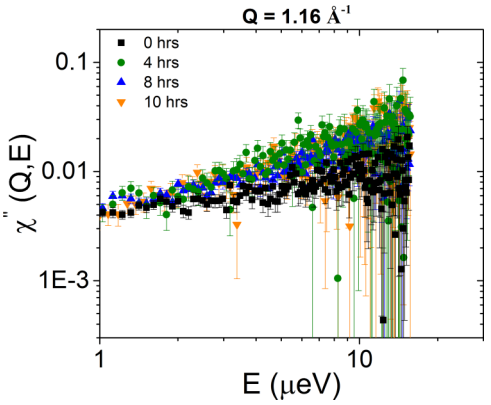

FIG. 5. Dynamic susceptibility (intensity divided by Bose factor) of QENS spectra at a representative Q of 1.16 $Å^{-1}$ showing a raising tail of the peak originating from the cation dynamics visible in the accessible dynamic range.

dynamics of hydrogen-bearing cations as [55]

$$S_{QE}(Q,\omega) = \frac{1}{\pi}\frac{\Gamma(Q)}{\omega^2 + \Gamma^2(Q)}, \tag{4}$$

where $\Gamma(Q)$ is the full width at half maximum (FWHM) of the Lorentzian peak. The full width at half maximum (FWHM) extracted from the fit [Figs. 3(b) and 3(c)], shows a clear Q dependence at low Q values, which becomes flattened at higher $Q's$, thus demonstrating a characteristic behavior of jump diffusion, therefore a Jump diffusion model [56] was used to fit the $\Gamma(Q)$ extracted using Eq. (4) as

$$\Gamma(Q) = \frac{DQ^2}{1 + DQ^2\tau_o}, \tag{5}$$

where (τ_o) is the residence time between jumps between two sites, and D is diffusion coefficient.

The jump diffusion [56] model fit, as represented by the solid lines in Fig. 4(a), yielded diffusion coefficients for different D_2O exposure times. Figure 4(b) shows the diffusion coefficient of cations as a function of water uptake. With no D_2O in the pores, the derived value $D = 0.52 \pm 0.01 \times 10^{-10}m^2\,s^{-1}$ is slightly higher than the diffusion coefficient reported for bulk ($D = 0.44 \pm 0.03 \times 10^{-10}m^2s^{-1}$) [57]. Note that the cation diffusivity in this CDC is ~5 times lower than the previously reported diffusivity values ($D = 2.45 \pm 0.2 \times 10^{-10}m^2\,s^{-1}$) in mesoporous (~8.8 nm) carbon [57]. This smaller value can be attributed to the cumulative effects of the smaller pores (0.7–3.1 nm) and the limited dynamic window of the HFBS [50], as evident from the raising tail of the dynamic susceptibility peak, but not its maximum (Fig. 5), as observed for all samples. Since the ions are sufficiently small, [$BMIm^+$][Tf_2N^-] likely fills both mesopores (>1 nm) and micropores (<1 nm). On the characteristic time scale (~10 ns) of the HFBS experiment resolution [50], the cations inside the micropores remain immobilized due to tight packing of ions inside the pore [58] and contribute only to the elastic signal. Therefore, measured dynamics account solely for the cations confined in the 3.1 nm pores. Narrow pores (1–3.1 nm), which preclude the formation of distinct high-density (immobilized ions at the pore wall-electrolyte interface) and low-density (center of pore) regions, may give rise to the more bulklike diffusion behavior of confined cations compared to the larger effect on the dynamics in the pores of 8.8 nm size [57]. The current result is consistent with the relationship between diffusivity in bulk and in confinement observed for ILs in silica monoliths with the pore sizes of 5–10 nm [59].

Even though [$BMIm^+$] has a long hydrophobic butyl (CH_3–CH_2–CH_2–CH_2–) chain and absorbs 0.26 wt. % water at 59% relative humidity [19], remarkably, our measurements show that the confined [$BMIm^+$][Tf_2N^-] absorbs significantly larger amount of water (~10 times) compared to the bulk liquid. Such water uptake yields a twofold diffusion coefficient increase after 4 h of D_2O exposure. This suggests that water molecules predominantly adsorb onto CDC surfaces and displace some of the adsorbed cations from their original sites on pore surfaces that leads to a decrease in elastic incoherent scattering fraction (EISF) [Fig. 4(b)] as a function of water uptake till the CDC pores become saturated. Those [$BMIm^+$] ions, which had been previously immobilized in the system, subsequently, demonstrate higher diffusivities. This observation may be fully analogous to the previously reported positive effect of water co-solvent on the diffusivity of methane confined in carbon aerogel [60]. It is worth noting here that even in the bulk state, addition of water increases the diffusivity of cation by reducing the cohesive attraction between the [$BMIm^+$][Tf_2N^-] molecules [61]. Therefore, overall increase in the diffusivity of cation could be the joint effect of ion displacement, as evident from a reduction in elastic intensity [Fig. 3(b)], and a possible screening of the attraction between the ionic liquid molecules by water. Furthermore, nearly similar values of residence times (Fig. 6), which is in a range of the characteristic times predicted by molecular dynamics simulations for the adsorption of ions of [$BMIm^+$][PF_6^-] on CDC [62], illustrate that the increase in diffusivity is due to an increase in the average jump length, consistent with a gradual decrease of cation density on the walls of the microspores.

After increasing the D_2O vapor exposure time to 8 h, D_2O uptake increased from 3.5 wt. % (1.3 mol D_2O per mol of IL) to 5.2 wt. % (1.9 mol D_2O per mol of IL). This yielded yet another twofold diffusion coefficient increase, likely due to the same displacement effect. However, after 10 h of D_2O vapor exposure and a substantially higher heavy water uptake (~20 wt.%, or 7.6 mol D_2O per mol of IL),

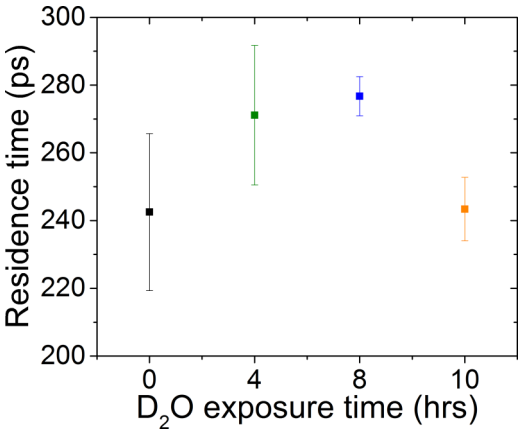

FIG. 6. Residence times extracted from a single Lorentzian fit of $S(Q, E)$ of the confined $[BMIm^+][Tf_2N^-]$ as a function of D_2O exposure time form the model fit.

we did not observe any further increase in cation diffusivity. We conclude that the $[BMIm^+][Tf_2N^-]$ filled pore surfaces became saturated with D_2O after 8 h of vapor exposure. For comparison, CDCs with unfilled pores can adsorb up to 35 wt. % of water relative to their dry mass, depending on the pore volume [63]. Since the CDC material in this study was treated with NH_3(g) after Cl_2(g) etching, it likely retained some nitrogen-containing groups (–NH_3,–NH_2, quaternary nitrogen) and chemisorbed oxygen [64,65]. Consequently, its surfaces were hydrophilic and accelerated water vapor uptake [43]. The observed increase in the microscopic diffusivity in $[BMIm^+][Tf_2N^-]$ with increasing water content may explain the greater electrochemical performance of the ionic liquid observed in water-containing pores from electrochemical measurements.

Molecular dynamics (MD) simulations were used to further investigate high water uptake in confined $[BMIm^+][Tf_2N^-]$ and humidity effects on cation dynamics. The simulation predicts greater water composition in pores than in bulk and, for low and moderate water concentrations, preferential arrangement on the pore walls due to defects introduced interactions, in contrast to depletion of water molecules observed in defect free graphene [66], over the center of the pore. Figure 7 shows snapshots of two MD simulations of water and $[BMIm^+][Tf_2N^-]$ confined in a model pore. Figure 8 quantifies this relationship: water composition inside the pore exceeds densities from comparable bulk simulations, whereas the water composition in the bulk region of the pore simulation boxes is smaller.

Figure 9 shows that, for low to moderate water concentrations, water accumulates on the pore walls and is absent from the middle regions of pores. At larger water concentrations, however, water saturates available pore surfaces and begins to accumulate in the pore centers. At such sample compositions, a relatively smaller fraction of ions is found on the pore walls. Accordingly, and similar to the QENS observation, MD simulations predict greater cation diffusivity upon addition of water. A summary is presented as an inset in Fig. 9, showing a relationship between cation diffusivity and water concentration for a model confined system.

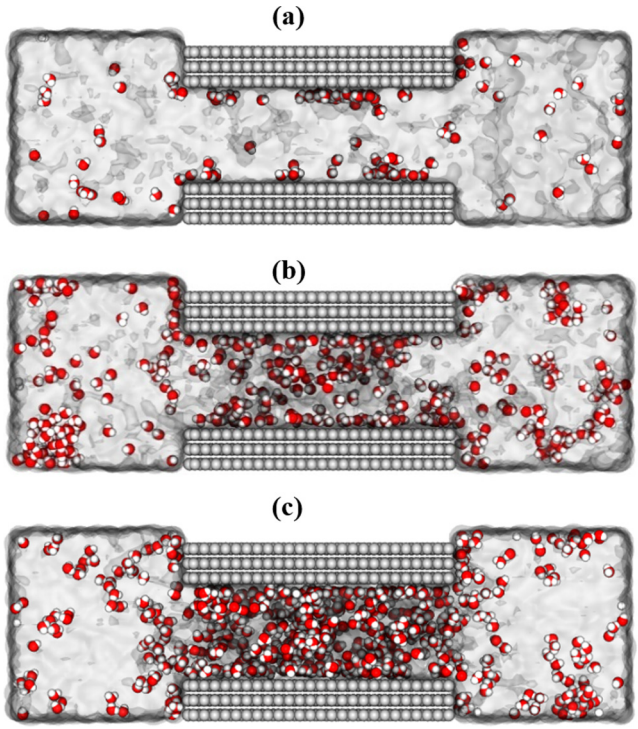

FIG. 7. Visualizations of representative snapshots of MD simulations of confined humid $[BMIm^+][Tf_2N^-]$. Carbon atoms making up pore walls are silver spheres and water molecules are drawn with conventional CPK coloring. For simplicity, ionic liquid molecules were represented with a surface model; they are not explicitly shown, but the area in which they fill is outlined with a transparent gray surface. Water composition in each image are (a) 0.2, (b) 0.48, and (c) 0.60 mole fraction with corresponding 1, 3.8, and 6.1 wt. %. At low water concentrations (a), some water is found in the bulk and those in the pore tend to prefer the pore wall. At moderate concentration (b), more water is found throughout, including filling the middle of the pore. Comparison of these images shows a stronger preference of water molecules to reside in the pore (both near the walls and in the middle), which implies that confinement increases the solubility of water in IL. The length of these MD simulations is sufficient for water molecules to sufficiently explore both regions of the simulation box. These results therefore imply that the solubility of water in confined IL exceeds that of bulk IL.

Comparison of the experimental cation diffusivities in Fig. 4(b) and the computed cation diffusivities in Fig. 9 inset reveals both the power and limitations of MD simulations, which compute system parameters in accordance with the assumed system composition. While the MD cation diffusivities for $X_w = 0$ and $X_w = 0.2$, where the water molecules are near the walls (Fig. 9), are in reasonable agreement with the experimental data, the MD cation diffusivities rise very quickly once, at higher concentrations, the water molecules start occupying the middle of the pore (Fig. 9). On the other hand, the saturation of the cation diffusivities observed in the experiment at higher water concentrations suggests that, in experimental samples, the water molecules occupy sites near the walls, but not the middle of the pores, and the progressively increasing water uptake with the prolonged exposure to vapors

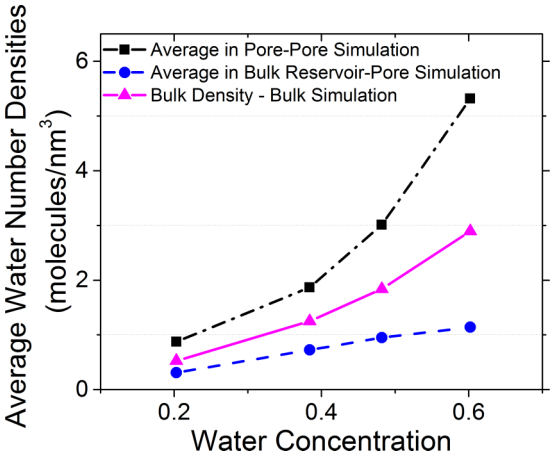

FIG. 8. Comparison of water densities in regions of pore simulation boxes compared to bulk densities in independent bulk simulations. To facilitate comparison, initial fluid compositions between compared simulations were equal. Throughout, the density of water inside the pore was greater than the bulk-like region of the pore simulations.

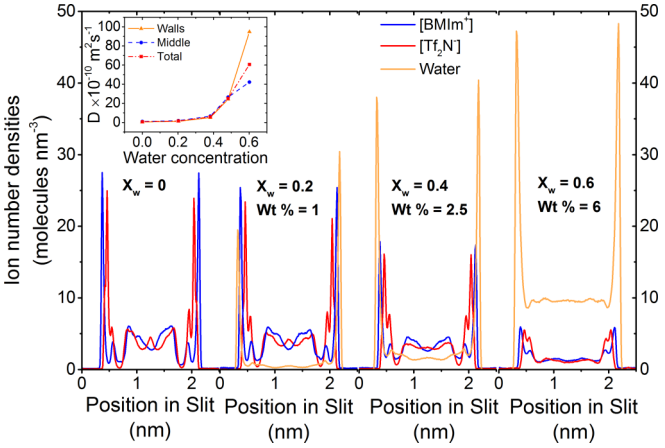

FIG. 9. Number density profiles of RTIL ions and water across the width of the model pore used in MD simulation at different mole fractions (X_w). Inset in the figure shows the relationship between cation diffusivity and water concentration. The energetic coefficient of the water-carbon interaction ($\varepsilon_{\text{water-wall}}$) has been doubled in each simulation. As water molecules are added to the simulations, they settle on the pore walls before filling the entire pore.

is due to water molecules going elsewhere in the sample after saturating the near-walls sites. The likely reason for that is the strong repulsive interactions between water molecules and the ionic liquid. These repulsive interactions would indeed result in high cation diffusivities, as observed in the simulations, if the water molecules could be mixed with the ionic liquid in the middle of the pores. This can be observed in the simulation, where the system composition is set up at will, but not necessarily in real samples, where, after the saturation of the near-wall sites by water molecules, further water uptake from the vapor could not get water molecules in the middle of the pores, in agreement with the well documented low miscibility of bulk ionic liquid with water. Once the water molecules in the simulation are introduced in sufficient concentrations to occupy the middle of the pores, the resulting cation diffusivities become much higher than those observed in the experiment, thus demonstrating that the water uptake in the real pores is limited to water molecules near the pore walls.

IV. CONCLUSION

We demonstrated the effect of water molecules on charge storage capabilities and microscopic dynamics of a RTIL confined in porous carbon electrodes. We propose that water did not simply solvate the hydrophobic [BMIm$^+$][Tf$_2$N$^-$], but instead acted as a secondary (impurity like) liquid system and displaced the ions from their locations along CDC surfaces. This net effect improved the self-diffusion and dynamics of the electrolyte species. Electrochemical testing correlated this finding with greater rate handling abilities and lower ionic impedance of the RTIL and, consequently, demonstrated the viability of this supercapacitor system in humid environments. The positive influence of water content on the charge storage densities within the stability window of the electrolyte parallels similar improvements to Na-ion [67] and Mg-ion [68,69] batteries. Future efforts must use a combination of experimental techniques and molecular simulations to assess water-RTIL interactions and investigate other pore geometries, electrolyte ions, and temperature effects.

ACKNOWLEDGMENTS

This work was supported as part of the Fluid Interface Reactions, Structures and Transport (FIRST) Center, an Energy Frontier Research Center funded by the U.S. Department of Energy, Office of Science, Office of Basic Energy Sciences. Work at ORNL's Spallation Neutron Source was supported by the U.S. Department of Energy, Office of Basic Energy Sciences. Oak Ridge National Laboratory is managed by UT-Battelle, LLC, for U.S. DOE under Contract No. DE-AC05-00OR22725. Experiments on HFBS at NIST Center for Neutron Research (NCNR) were supported in part by the National Science Foundation under Agreement No. DMR-1508249. Certain commercial material suppliers are identified in this paper to foster understanding. Such identification does not imply recommendation or endorsement by the National Institute of Standards and Technology, nor does it imply that the materials or equipment identified are necessarily the best available for the purpose.

[1] P. Simon, Y. Gogotsi, and B. Dunn, Science **343**, 1210 (2014).
[2] P. Simon and Y. Gogotsi, Acc. Chem. Res. **46**, 1094 (2013).
[3] C. L. Wang, Y. Zhou, L. Sun, P. Wan, X. Zhang, and J. S. Qiu, J. Power Sources **239**, 81 (2013).
[4] I. E. Rauda, V. Augustyn, B. Dunn, and S. H. Tolbert, Acc. Chem. Res. **46**, 1113 (2013).
[5] Y. W. Zhu, S. Murali, M. D. Stoller, K. J. Ganesh, W. W. Cai, P. J. Ferreira, A. Pirkle, R. M. Wallace, K. A. Cychosz,

M. Thommes, D. Su, E. A. Stach, and R. S. Ruoff, Science **332**, 1537 (2011).
[6] Y. Gogotsi, MRS Bull. **40**, 1110 (2015).
[7] F. Béguin, V. Presser, A. Balducci, and E. Frackowiak, Adv. Mater. **26**, 2219 (2014).
[8] K. Fic, G. Lota, M. Meller, and E. Frackowiak, Energy Environ. Sci. **5**, 5842 (2012).
[9] T. Brousse and D. Belanger, Electrochem. Solid-State Lett. **6**, A244 (2003).
[10] P. Kurzweil and M. Chwistek, J. Power Sources **176**, 555 (2008).
[11] T. Sato, G. Masuda, and K. Takagi, Electrochim. Acta **49**, 3603 (2004).
[12] K. L. Van Aken, M. Beidaghi, and Y. Gogotsi, Angew. Chem. Int. Ed. **54**, 4806 (2015).
[13] S. Kondrat, C. R. Perez, V. Presser, Y. Gogotsi, and A. A. Kornyshev, Energy Environ. Sci. **5**, 6474 (2012).
[14] N. N. Rajput, J. Monk, R. Singh, and F. R. Hung, J. Phys. Chem. C **116**, 5169 (2012).
[15] N. C. Osti, K. L. Van Aken, M. W. Thompson, F. Tiet, D. E. Jiang, P. T. Cummings, Y. Gogotsi, and E. Mamontov, J. Phys. Chem. Lett. **8**, 167 (2017).
[16] N. D. Khupse and A. Kumar, J. Solution Chem. **38**, 589 (2009).
[17] R. Lin, P. Huang, J. Segalini, C. Largeot, P. L. Taberna, J. Chmiola, Y. Gogotsi, and P. Simon, Electrochim. Acta **54**, 7025 (2009).
[18] C. Zhao, A. M. Bond, and X. Lu, Anal. Chem. **84**, 2784 (2012).
[19] L. Cammarata, S. G. Kazarian, P. A. Salter, and T. Welton, Phys. Chem. Chem. Phys. **3**, 5192 (2001).
[20] C. D. Tran, S. H. D. Lacerda, and D. Oliveira, Appl. Spectrosc. **57**, 152 (2003).
[21] H. V. Spohr and G. N. Patey, J. Chem. Phys. **132**, 154504 (2010).
[22] A. Triolo, O. Russina, H.-J. Bleif, and E. Di Cola, J. Phys. Chem. B **111**, 4641 (2007).
[23] A. L. Sturlaugson, K. S. Fruchey, and M. D. Fayer, J. Phys. Chem. B **116**, 1777 (2012).
[24] Y. Cao, Y. Chen, X. Wang, and T. Mu, RSC Adv. **4**, 5169 (2014).
[25] M. Rose, Y. Korenblit, E. Kockrick, L. Borchardt, M. Oschatz, S. Kaskel, and G. Yushin, Small **7**, 1108 (2011).
[26] J. Biener, M. Stadermann, M. Suss, M. A. Worsley, M. M. Biener, K. A. Rose, and T. F. Baumann, Energy Environ. Sci. **4**, 656 (2011).
[27] V. Presser, M. Heon, and Y. Gogotsi, Adv. Funct. Mater. **21**, 810 (2011).
[28] S. Brunauer, P. H. Emmett, and E. Teller, J. Am. Chem. Soc. **60**, 309 (1938).
[29] G. Y. Gor, M. Thommes, K. A. Cychosz, and A. V. Neimark, Carbon **50**, 1583 (2012).
[30] P. L. Taberna, P. Simon, and J. F. Fauvarque, J. Electrochem. Soc. **150**, A292 (2003).
[31] P. L. Taberna, C. Portet, and P. Simon, Appl. Phys. A **82**, 639 (2006).
[32] J. Segalini, B. Daffos, P. L. Taberna, Y. Gogotsi, and P. Simon, Electrochim. Acta **55**, 7489 (2010).
[33] B. Dyatkin and Y. Gogotsi, Faraday Discuss. **172**, 139 (2014).
[34] P. C. Hillesheim, J. A. Singh, S. M. Mahurin, P. F. Fulvio, Y. Oyola, X. Zhu, D.-e. Jiang, and S. Dai, RSC Adv. **3**, 3981 (2013).
[35] J. L. Bañuelos, G. Feng, P. F. Fulvio, S. Li, G. Rother, S. Dai, P. T. Cummings, and D. J. Wesolowski, Chem. Mater. **26**, 1144 (2014).
[36] J. L. Bañuelos, G. Feng, P. F. Fulvio, S. Li, G. Rother, N. Arend, A. Faraone, S. Dai, P. T. Cummings, and D. J. Wesolowski, Carbon **78**, 415 (2014).
[37] M. J. Abraham, T. Murtola, R. Schulz, S. Páll, J. C. Smith, B. Hess, and E. Lindahl, SoftwareX **1**, 19 (2015).
[38] J. N. C. Lopes, J. Deschamps, and A. A. H. Padua, J. Phys. Chem. B **108**, 2038 (2004).
[39] J. N. C. Lopes and A. A. H. Padua, J. Phys. Chem. B **110**, 19586 (2006).
[40] Y. Zhang and E. J. Maginn, J. Phys. Chem. B **116**, 10036 (2012).
[41] W. L. Jorgensen, J. Chandrasekhar, J. D. Madura, R. W. Impey, and M. L. Klein, J. Chem. Phys. **79**, 926 (1983).
[42] G. Bussi, D. Donadio, and M. Parrinello, J. Chem. Phys. **126**, 014101 (2007).
[43] B. Dyatkin, E. Mamontov, K. M. Cook, and Y. Gogotsi, Prog. Nat. Sci.: Mater. Int. **25**, 631 (2015).
[44] L. Martinez, R. Andrade, E. G. Birgin, and J. M. Martinez, J. Comput. Chem. **30**, 2157 (2009).
[45] H. S. Kim, J. P. Singer, Y. Gogotsi, and J. E. Fischer, Microporous Mesoporous Mater. **120**, 267 (2009).
[46] M. D. Stoller and R. S. Ruoff, Energy Environ. Sci. **3**, 1294 (2010).
[47] V. Gau, S.-C. Ma, H. Wang, J. Tsukuda, J. Kibler, and D. A. Haake, Methods **37**, 73 (2005).
[48] E. Mamontov and K. W. Herwig, Rev. Sci. Instrum. **82**, 085109 (2011).
[49] S. M. Mahurin, E. Mamontov, M. W. Thompson, P. Zhang, C. H. Turner, P. T. Cummings, and S. Dai, Appl. Phys. Lett. **109**, 143111 (2016).
[50] A. Meyer, R. Dimeo, P. Gehring, and D. Neumann, Rev. Sci. Instrum. **74**, 2759 (2003).
[51] V. F. Sears, Neutron News **3**, 26 (1992).
[52] R. T. Azuah, L. R. Kneller, Y. M. Qiu, P. L. W. Tregenna-Piggott, C. M. Brown, J. R. D. Copley, and R. M. Dimeo, J. Res. Natl. Inst. Stand. Technol. **114**, 341 (2009).
[53] M. Bee, *Quasi-elastic Neutron Scattering* (Adam Hilger, Bristol, 1998).
[54] M. Tyagi, A. Alegria, and J. Colmenero, J. Chem. Phys. **122**, 244909 (2005).
[55] N. C. Osti, A. Cote, E. Mamontov, A. Ramirez-Cuesta, D. J. Wesolowski, and S. O. Diallo, Chem. Phys. **465**, 1 (2016).
[56] K. Singwi and A. Sjölander, Phys. Rev. **119**, 863 (1960).
[57] S. M. Chathoth, E. Mamontov, S. Dai, X. Wang, P. F. Fulvio, and D. J. Wesolowski, Europhys. Lett. **97**, 66004 (2012).
[58] Y. He, R. Qiao, J. Vatamanu, O. Borodin, D. Bedrov, J. Huang, and B. G. Sumpter, J. Phys. Chem. Lett. **7**, 36 (2016).
[59] R. Goebel, P. Hesemann, J. Weber, E. Moller, A. Friedrich, S. Beuermann, and A. Taubert, Phys. Chem. Chem. Phys. **11**, 3653 (2009).
[60] S. M. Chathoth, E. Mamontov, Y. B. Melnichenko, and M. Zamponi, Microporous Mesoporous Mater. **132**, 148 (2010).
[61] A. L. Rollet, P. Porion, M. Vaultier, I. Billard, M. Deschamps, C. Bessada, and L. Jouvensal, J. Phys. Chem. B **111**, 11888 (2007).
[62] C. Pean, B. Daffos, B. Rotenberg, P. Levitz, M. Haefele, P. L. Taberna, P. Simon, and M. Salanne, J. Am. Chem. Soc. **137**, 12627 (2015).

[63] M. McNallan and P. Gupta, ECS Trans. **6**, 71 (2007).
[64] D. Hulicova-Jurcakova, M. Seredych, G. Q. Lu, and T. J. Bandosz, Adv. Funct. Mater. **19**, 438 (2009).
[65] J. L. Figueiredo, M. F. R. Pereira, M. M. A. Freitas, and J. J. M. Órfão, Carbon **37**, 1379 (1999).
[66] G. Feng, X. Jiang, R. Qiao, and A. A. Komyshev, ACS Nano **8**, 11685 (2014).
[67] K. W. Nam, S. Kim, E. Yang, Y. Jung, E. Levi, D. Aurbach, and J. W. Choi, Chem. Mater. **27**, 3721 (2015).
[68] K. W. Nam, S. Kim, S. Lee, M. Salama, I. Shterenberg, Y. Gofer, J.-S. Kim, E. Yang, C. S. Park, J.-S. Kim, S.-S. Lee, W.-S. Chang, S.-G. Doo, Y. N. Jo, Y. Jung, D. Aurbach, and J. W. Choi, Nano Lett. **15**, 4071 (2015).
[69] J. Song, M. Noked, E. Gillette, J. Duay, G. Rubloff, and S. B. Lee, Phys. Chem. Chem. Phys. **17**, 5256 (2015).